

This item is the archived peer-reviewed author-version of:

Real-time structured light profilometry : a review

Reference:

van der Jeught Sam, Dirckx Joris.- Real-time structured light profilometry : a review
Optics and lasers in engineering - ISSN 0143-8166 - (2016), p. 1-31

1 **Real-time structured light profilometry: a review**

2 Sam Van der Jeught^{a,*} & Joris J.J. Dirckx^a

3 ^aLaboratory of Biomedical Physics (BIMEF), University of Antwerp, Groenenborgerlaan 171, B-
4 2020 Antwerp, Belgium.

5 * Correspondence to: sam.vanderjeught@ua.ac.be

6 **Abstract:**

7 The acquisition of high-resolution, real-time three-dimensional surface data of dynamically
8 moving objects has large applicability in many fields. When additional restrictions such as non-
9 invasiveness and non-contact measurement are imposed on the employed profilometry
10 technique, the list of possible candidates is reduced mainly to the broad range of structured light
11 profilometry methods. In this manuscript, the current state-of-the-art in structured light
12 profilometry systems is described, as well as the main advancements in hardware technology and
13 coding strategy that have led to their successful development. A chronological overview of
14 optical profilometry systems that have been reported to perform real-time acquisition, digital
15 signal processing and display of full-field 3D surface maps is presented. The respective operating
16 principles, strengths and weaknesses of these setups are reviewed and the main limitations and
17 future challenges in high-speed optical profilometry are discussed.

18 **Keywords:**

19 Real-time; structured light profilometry; review; phase unwrapping.

20

21

22

23

24

25

26

27

28

29 **1. Introduction**

30 With recent technological advancements in digital projection, imaging and processing hardware,
31 optical surface measurement techniques have evolved rapidly. The demand for non-contact,
32 high-resolution and fast 3D-shape measurement systems is propelled by the medical, industrial
33 and entertainment sector and has driven manufacturers and academic research groups to design a
34 wide variety of optical profilometry techniques. Generally, they vary in terms of hardware
35 configuration, stability, cost, resolution and speed.

36 *Time-of-flight* profilometers [1–3] measure the time required for a light pulse to travel from the
37 transmitter to an object and back to the receiver. The object surface is scanned point-per-point in
38 an array of arbitrarily dense sampling points and a depth map is created subsequently. Time-of-
39 flight methods are generally stable, straightforward 3D-measurement techniques and require no
40 calibration to produce absolute depth data. However, axial measurement accuracy (typically 0.1-
41 1 cm) is limited to the temporal resolution of the transmitter-receiver system and cannot be
42 improved through optical magnification.

43 *Image-based* techniques analyze how an image is formed and how lighting affects the objects
44 within that image. Three-dimensional surface information is extracted from the two-dimensional
45 representation of the object through (complicated) image analysis. *Shape-from-shading* methods
46 [4,5] recover the surface shape from the image by modeling the gradual variations of grayscale
47 shading in the image and by determining each pixel's relative distance to the imaging source.
48 *Shape-from-focus-and-defocus* methods [6,7] recover the surface shape by correlating the degree
49 of local blur on the object to relative distance from the imaging lens. *Stereo vision* profilometry
50 techniques [8,9] simulate the stereoscopic setup of human vision by employing a second camera
51 placed at an angle with the original camera. Identifying common features on the object in images
52 taken from multiple perspectives or *stereo-matching* allows the object surface shape to be
53 reconstructed using standard triangulation techniques. Image-based profilometry techniques
54 require only a digital camera (or two, in the case of stereo vision techniques) and are generally
55 low-cost setups. However, limited measurement accuracy in depth and computationally intensive
56 digital signal processing requirements reduce their usability in real-time profilometric setups.

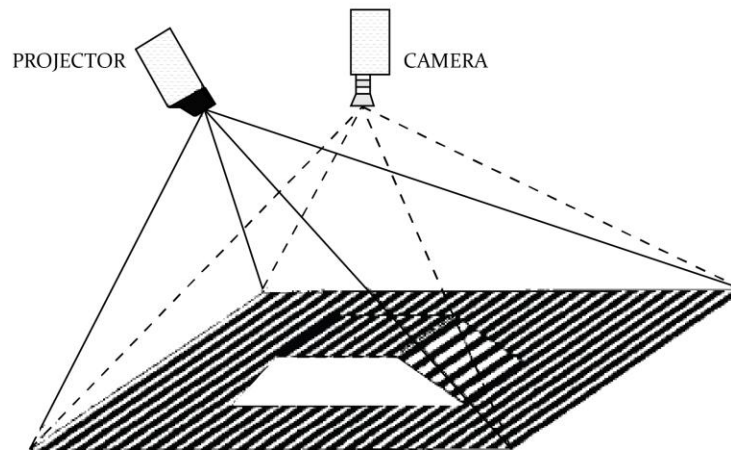
57 Similar to stereo-vision profilometry, *Moiré profilometry* [10,11] requires an additional optical
58 axis in its setup design. By replacing one of the two cameras with a projection device to
59 illuminate the object with structured light patterns, one can avoid the stereo-matching problem.
60 When observed under an angle, the projected patterns are deformed by the object's surface
61 shape. In Moiré profilometry, mechanical interference is induced by placing a demodulation grid
62 - identical but slightly misaligned to the original projection grid - between the object and the
63 camera. Contours of equal height can then be extracted from the resulting interference pattern.
64 Practically, however, the need for a physical demodulation grid complicates the hardware
65 configuration of the experimental setup.

66 More recently, various *structured light projection* (SLP) techniques have been reported that
67 employ the same projector-camera setup as Moiré techniques but lack the demodulation grid.
68 Instead, surface height information is extracted directly from analysis of the deformed grid
69 pattern. By eliminating the demodulation grid, SLP techniques allow for a more straightforward
70 and stable experimental setup to be designed. In addition, specific depth extraction can be
71 performed in a number of ways, depending on the nature and the amount of projected patterns.

72 The remainder of the paper is structured as follows: in Section 2, the broad range of structured
73 light profilometry techniques is subdivided according to general coding strategy, briefly
74 describing their respective operating principles and highlighting their potential applicability in
75 real-time setups. Section 3 discusses the associated problem of phase unwrapping. In Section 4,
76 we give an overview of SLP systems that have been reported to operate in real-time and describe
77 the main advances in digital projection technology and coding strategy that have led to their
78 development. Section 5 discusses the strengths and weaknesses of single-shot versus multi-shot
79 techniques in high-speed setups, summarizes the current limitations of state-of-the-art SLP
80 techniques and describes future challenges. Finally, Section 6 concludes the paper.

81 **2. Structured light profilometry techniques**

82 The low-cost access to fast, high-resolution digital projection systems based on liquid crystal
83 displays (LCD) and digital light projectors (DLP) has enabled the development of a wide variety
84 of structured light profilometry techniques. Structured light or active illumination profilometry
85 techniques illuminate the measurement object with predefined spatially varying intensity patterns
86 and record these patterns as they are deformed by the object shape when observed at an angle
87 with the projection axis. The basic setup of SLP techniques is illustrated in Figure 1. A structured
88 light modulator (*projector*) projects the pattern onto the scene and an imaging sensor (*camera*)
89 placed at a relative angle with the projection axis records the deformed pattern. Digitalization of
90 this basic projector-camera setup has enabled numerous SLP-techniques to be developed, each
91 with their own respective strengths and weaknesses.

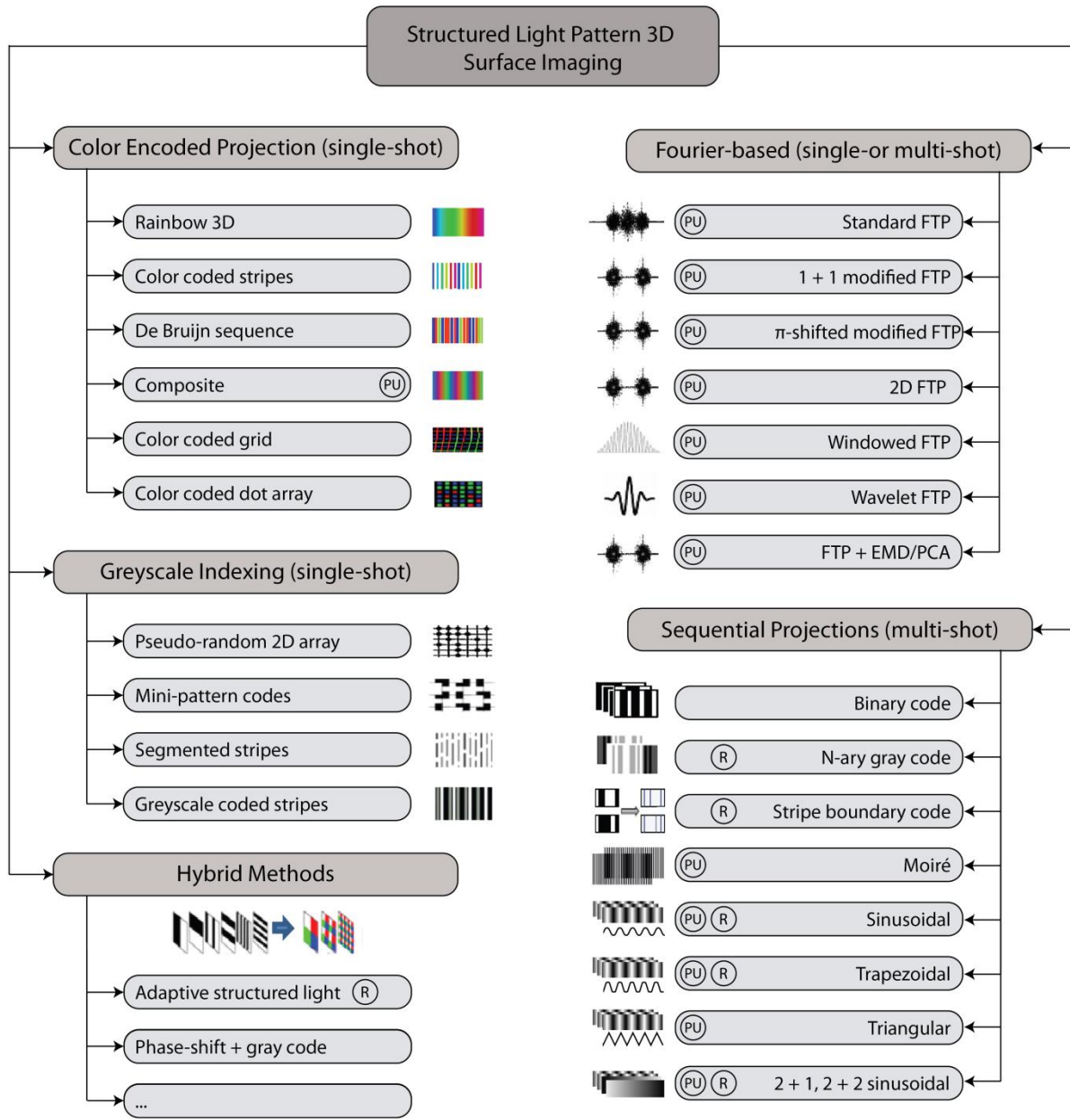


92

93 Figure 1: Standard projector-camera configuration used in structured light profilometry
94 techniques. Figure modified from Sansoni et al. [12].

95 Though they are all unique in their specific implementation, differentiation between them can be
96 made based on whether or not they require multiple projected patterns per 3D measurement
97 (single-shot versus multi-shot techniques), whether or not they use color encoded projection
98 schemes, and specific coding strategy. A more precise schematic overview of the different
99 classes of structured light projection techniques is presented in Figure 2, analogous to the
100 overview created by Geng [13]. Here, we have updated the overview with recently developed

101 techniques, added the family of Fourier-based profilometry techniques and subdivided the set of
 102 phase shifting techniques according to their respective projected intensity profiles. Techniques
 103 which have been reported to reach real-time (>10 3D frames per second) acquisition, digital
 104 signal processing and display of 3D surface maps are marked with an encircled 'R'-symbol.
 105 Techniques which require phase unwrapping (see Section 3) as part of their reconstruction
 106 algorithm are marked with an encircled 'PU'-symbol.



107
 108 Figure 2: (color online) Schematic overview of structured light profilometry techniques.
 109 Techniques that require phase unwrapping are marked with an encircled 'PU'-symbol,
 110 techniques that have been implemented in real-time are marked with an encircled 'R'-symbol.

111 2.1 Color encoded projection techniques

112 Color encoded projection techniques employ color as a differentiating tool to uniquely label the
113 object surface. The major advantage of color encoded projection techniques is their potential
114 ability to acquire depth information using only a single projected image. Their disadvantage,
115 however, lies in the fact that a color-independent reflectivity profile of the measurement target is
116 assumed and that the quality of the resulting depth map is greatly influenced by the
117 correspondence between projected and recorded color values. This makes them often unsuitable
118 for practical applications that need to measure (partly) colored objects.

119 *Rainbow 3D* cameras [14,15] illuminate the object with a spatially varying color pattern,
120 establishing a one-to-one correspondence between the projection angle and a particular
121 wavelength. This way, each surface point is landmarked with a specific wavelength and can be
122 triangulated if the angle between the projection and camera axes is known. This technique is
123 highly sensitive to the dynamic range and color resolution of the employed CCD chip: with a
124 standard image sensor containing three 8-bit channels, a total of 2^{24} different colors can be
125 represented. Correct triangulation implies a one-to-one correspondence between projected and
126 recorded color value over this entire color range, making rainbow 3D cameras highly sensitive to
127 cross-talk between color channels. By projecting *color coded stripes* [16] onto the target surface,
128 the range of the color-sensitive CCD chip can be subdivided in discrete levels, reducing the in-
129 plane resolution but making the technique more robust to color-dependent reflectivity profiles. A
130 special color coded stripe sequence is based on the unique features of a *De Bruijn sequence*
131 [17,18]. A De Bruijn sequence of rank n on a base set of size k is a cyclic word in which each of
132 the k^n words of length n appears exactly once as we travel through the cycle. This way, a stripe
133 pattern can be constructed that consists of uniquely identifiable local color patterns with a limited
134 set of base colors. *Composite* color coding techniques superimpose multiple phase shifted
135 patterns onto a single color image [19,20]. This color pattern is then projected onto the target
136 statically and is recorded by a color-sensitive CCD chip. By separating the color channels in
137 post-processing, the deformed phase shifted patterns can be reconstructed and the object height
138 profile can be extracted using well-known phase shifting techniques. A combination of color
139 coded stripes and composite color coding techniques consists of encoding multiple patterns into
140 a single color projection image. This way, the ambiguity problem caused by employing phase
141 shifted patterns can be alleviated [21,22]. In any case, one should reduce the decoding error rate
142 by optimizing the color sets by maximizing the distance between adjacent colors in the projected
143 pattern. Another type of color encoding strategy is to project both horizontal and vertical stripes
144 onto the target so that a *color coded grid* is achieved. Adding this extra dimension of encoding
145 facilitates solving the correspondence problem [23,24], although the limited thickness of the
146 projected lines reduces the stability of this technique when compared to the above color encoded
147 methods. Similarly, a *color coded dot array* of pseudo-randomized colored pixels can be used to
148 encode the object surface with a 2D color pattern. Brute force algorithms [25,26] have been used
149 to ensure the uniqueness of subwindows of predefined size, though it has been reported that not
150 all possible subwindow patterns may be exhausted [13].

151 2.2 Grayscale indexing

152 Grayscale indexing methods are single-shot techniques that project a series of dots, stripes or
153 coded patterns onto the target and employ pattern search algorithms to solve the correspondence

154 problem and to reconstruct the 3D object shape. They are color-independent methods which can
155 be used to measure objects that contain non-uniform surface color distributions. On the other
156 hand, as these techniques typically rely on recovering the deformed projected pattern within at
157 least a subwindow of the projected pattern, they are sensitive to object surface discontinuities
158 and require high in-plane resolving power.

159 One indexing strategy is to label the object surface with a *pseudo-random binary array* (PRBA)
160 that contains binary dots on some of the intersections of a Cartesian grid [25,27]. By constructing
161 the PRBA so that every subwindow of the projected pattern is unique, every coordinate location
162 can be uniquely determined. Deformation of the 2D Cartesian dot pattern can then be used to
163 triangulate the object depth at every intersection of the projected grid. Alternatively, *mini-*
164 *patterns* can be used as code words to form a grid-indexed projection pattern [28] by arranging a
165 set of mini-patterns in a pseudo-random 2D array so that every subwindow is unique. In analogy
166 with the projection of color coded stripes, binary stripes can be labeled by adding cuts at different
167 predefined positions, dividing them in uniquely identifiable segment series [29]. This technique
168 is commonly referred to as *segmented stripes* profilometry. Finally, *grayscale coded stripes* can
169 be repeated in a pattern if more than two intensity levels are used. By arranging them such that
170 any group of stripes within a certain period of length is unique, a pattern matching algorithm can
171 be used to locate the individual deformed stripes [30].

172 **2.3 Fourier-based profilometry**

173 Another subset of grayscale SLP techniques that require only a single frame to retrieve the 3D
174 object surface profile is the group of Fourier transform profilometry (FTP) techniques. In
175 contrast to the grayscale indexing methods that project uniquely identifiable patterns onto the
176 object, FTP techniques typically employ standard sinusoidal or *Ronchi* gratings to cover the
177 entire object surface. This makes them less sensitive to image defocus when compared to
178 indexing methods. On the other hand, as successful 3D reconstruction is determined by the
179 correct selection of only the originally projected or *fundamental* frequency band in Fourier space,
180 FTP techniques are nevertheless limited to a finite maximum slope of depth variation. Beyond
181 this maximum, the fundamental frequency band overlaps the zero component and other high
182 frequency components and cannot be retrieved unambiguously [31,32].

183 Originally, *standard FTP* was introduced by Takeda et al. [33] in 1982. Sinusoidal gratings are
184 projected onto the object and appear deformed by the object surface shape when observed at an
185 angle with the projection axis. Next, the obtained image is Fourier transformed row-per-row in
186 the direction perpendicular to the projected patterns and the frequency spectrum is filtered to
187 properly isolate the fundamental frequency which is broadened to a frequency band by the non-
188 uniform slope distribution of the object surface shape. Inverse Fourier transform of only this
189 frequency band results in a principle phase value ranging from $-\pi$ to π . After phase unwrapping
190 (see below) and calibration, these phase values can be linked to the actual object depth.

191 In order to decrease overlapping with frequencies caused by features such as shadows, non-
192 uniformities or contours that are present on the object surface itself, *1+1 modified FTP*
193 techniques [34] record an additional image of the measurement target before projecting the
194 Ronchi gratings. By subtracting this background image from the image containing the projected
195 lines, only the deformed lines remain and the fundamental frequency band can be selected more
196 easily from the obtained spectra. While this procedure significantly increases the measurement

197 precision of the FTP technique, it does not completely remove frequency overlapping and
198 requires an additional reference image of the uniformly lit target. Similarly, *π -shifted modified*
199 *FTP* techniques [35] record an additional frame of the measurement target after the projected
200 gratings are shifted over half a period. This way, the fundamental spectrum modulated by the
201 object height distribution can theoretically be extended from 0 to $2\nu_0$, where ν_0 is the
202 fundamental carrier frequency, without overlapping the zero- or higher frequency components.
203 When measuring coarse objects with surface discontinuities or speckle-like structures, local loss
204 of contrast around the projected fringes can hinder the row-per-row reconstruction of object
205 phase. In order to accomplish automatic depth measurement of such objects, one might employ
206 *two-dimensional (2D) FTP* techniques [36]. These techniques perform a two-dimensional
207 Fourier transform of the entire observed fringe pattern, filter the resulting spectrum by a 2D
208 Hanning window and perform an inverse Fourier transform to retrieve the object phase. It was
209 demonstrated that 2D FTP techniques provide better separation of the fundamental frequencies
210 from noise and diminishes the effect of local surface discontinuities on the resulting 3D depth
211 measurement [37]. Alternatively, *windowed FTP* techniques [38–40] divide the entire fringe
212 pattern into a limited set of local fringe regions by using a moving window. Next, each segment
213 is Fourier transformed and all local spectra are superimposed to retrieve the entire fringe
214 pattern's spectrum. By optimizing the window function and the projected fringe period to the
215 specific measurement object surface, the effect of fringe noise can be suppressed and spectral
216 leakage caused by local discontinuities in the fringe pattern can be reduced. Obviously, the
217 computational cost of windowed FTP is significantly greater than that of standard FTP
218 techniques. *Wavelet transform profilometry* techniques [41,42] also separate the signal in
219 segments, but change the window function according to the local frequency. Typically, 1D *Paul*
220 or *Morlet* mother wavelets are used [43] but 2D continuous wavelets have been reported as well
221 [44,45]. In comparison to the Fourier transform, wavelet transforms are computationally more
222 expensive, but can better detect the local characteristics of the fringe pattern which results in
223 better measurement precision [40]. *Shearlets*, the natural extension of wavelets that were
224 designed to better accommodate anisotropic features such as edges or borders in images, have
225 recently been introduced in single-shot structured light profilometry [46]. It has been
226 demonstrated that their superior directional sensitivity allows for better distinction between noise
227 and fringes and improved general background removal [47]. Finally, *empirical mode*
228 *decomposition (EMD)* [48,49] or *principle component analysis (PCA)* [50] techniques were
229 introduced in FTP to extract the fundamental frequency band and to remove the non-linear
230 carrier frequency caused by divergent illumination without the need for capturing multiple fringe
231 patterns. With these methods, the recorded fringe patterns are adaptively decomposed into a
232 finite number of intrinsic mode functions or principle components by using algorithms that are
233 commonly referred to as sifting processes. This way, high frequencies can be separated from low
234 frequencies and the zero-spectrum can be extracted more precisely [32].

235 **2.4 Sequential projection techniques**

236 Although the above methods have the distinct advantage of being single-shot techniques, their
237 technical feasibility is often complicated by the specific reflective properties of the measurement
238 target. Many objects cannot guarantee color-independent reflectivity profiles and limit the
239 applicability of color encoded techniques. Similarly, a poorly reflecting surface layer drastically
240 limits the resolution of methods which rely on the exact reconstruction of coded mini-patterns,
241 binary dots or stripes from the acquired image. Finally, the measurement precision of FTP

242 techniques suffers when the measurement object has a non-uniform or non-diffusely reflecting
243 surface structure.

244 Consequently, speed may be sacrificed in favor of resolution and stability by using multi-shot
245 techniques. Multi-shot or sequential projection techniques acquire multiple images of the object
246 per 3D-measurement in a sequence of varying projected patterns.

247 The most straightforward multi-shot approach is to provide each point on the object surface with
248 a unique *binary code* by illuminating it with a sequence of black and white horizontal and
249 vertical stripes and extracting the depth information by matching the binary code words between
250 the original and the deformed sequence [51]. Optimally, N binary patterns can generate $2N$
251 different code words per image dimension. This means that the binary coding technique requires
252 a minimum of $2\log_2(512) = 18$ different projected patterns to uniquely describe a grid of $512 \times$
253 512 pixels. By dividing the projected intensities in M grayscale levels, N grayscale patterns can
254 generate MN different code words per image direction. This way, *gray code* profilometry [52]
255 can effectively increase the measurement speed of the profilometry technique by reducing the
256 minimum amount of required patterns per image dimension. Binary code and gray code
257 profilometry are generally robust techniques with relatively high tolerance for measurement
258 noise since only discretized intensity regions are used in all pixels. On the other hand, the large
259 amount of required frames per measurement significantly limits the acquisition speed.
260 Furthermore, the height map produced by both binary and gray code profilometry techniques is
261 determined by the successful detection of the smallest projected elements. Therefore, axial
262 resolution and transversal resolving power of the imaging sensor are inherently coupled. Similar
263 to binary code profilometry, *stripe boundary code* techniques [53,54] project a set of black and
264 white illumination patterns onto the measurement target. Unlike binary (and gray) code
265 techniques, however, stripe boundary code profilometry is based on time-codification of the
266 boundaries between projected stripes. As these boundaries are tracked between subsequent
267 frames, depth extraction is permitted even in the presence of moving objects in the scene. The
268 incorporation of temporal coherence between subsequent frames within a single measurement
269 cycle enables inter-frame tracking of object movement and limits motion artifacts in the
270 reconstruction of the 3D surface shape model.

271 In order to increase axial resolution whilst limiting the required number of frames per 3D-
272 measurement, phase shifting profilometry techniques [55–57] employ the entire dynamic range
273 of the projector-camera system. In phase shifting profilometry, a sequence of fringe patterns with
274 spatially varying intensity profiles and relative phase shifts between them are projected onto the
275 object. The phase shifts caused by the non-planar object surface are extracted from the acquired
276 deformed fringe patterns by calculating the relative intensity values pixel-per-pixel. Because they
277 are *intensity ratio*-based techniques, phase shifting profilometry methods are generally well-
278 suited to measure objects with poor overall or local reflective properties. The periodic nature of
279 the technique, however, introduces the problem of ambiguous phase extraction and requires
280 additional phase unwrapping calculations to retrieve the continuous phase map. This process is
281 discussed below in Section 3.

282 Originally, phase shifting profilometry techniques employed a second demodulation grid which
283 was placed between object and camera. When two (or more) slightly misaligned periodic arrays
284 are superimposed onto the camera chip, their respective spatial frequency differences form a beat

285 pattern commonly referred to as a *Moiré* pattern. If the projection and demodulation grid contain
286 gratings with spatial pitches P_p and P_d , respectively, the pitch of the resulting Moiré interference
287 fringes is increased to $P_p P_d / |P_p - P_d|$. This way, the camera does not need to resolve the projected
288 grid lines individually and a relatively low-resolution camera can be employed. The earlier
289 *shadow Moiré*-techniques [10,58] extracted height information from the interference pattern
290 between the projection grid and its shadow on the object surface. Phase shifting was then
291 performed by mechanically translating the object in the z-direction, causing the shadow lines to
292 shift laterally. Alternatively, a second (different) grid was used between object and camera to
293 demodulate the projected fringe pattern [59,60]. Relative phase-stepping was then achieved by
294 laterally translating the projection and/or demodulation grid. Later, *projection Moiré*-techniques
295 employed digital light projectors to directly project phase-shifted light patterns onto the object
296 surface [61]. The deformed light patterns are then demodulated by a grating which is placed in
297 front of the camera. Relative phase shifts between successive grating projections can now be
298 controlled in software using the digital light projector. More recently, LCD grids have been used
299 as both modulating and demodulating gratings [62–64] and the two-dimensional array of camera
300 pixels itself has been used as a sub-or super-sampled demodulation grid [65].

301 With the increased availability of high-resolution, high dynamic range CCD-cameras, recent
302 techniques have been developed that lack the second demodulation grid, but rather extract object
303 depth information through direct analysis of the deformed grid patterns. Traditionally, these grid
304 patterns have *sinusoidal* intensity profiles and the phase is recovered through calculation of an
305 arctangent function. In order to replace the computationally time-consuming arctangent function
306 with a straightforward intensity ratio calculation, Zhang et al. proposed a new three-step phase
307 shifting algorithm which employed grids with *trapezoidal* intensity profiles [56,66]. As these
308 patterns defocus and converge toward sinusoids over large object depths, the resulting phase
309 errors are compensated by use of a lookup table. Both sinusoidal and trapezoidal phase shifting
310 techniques require three or more images to correctly extract phase information. In contrast,
311 *triangular* phase-shifting algorithms are able to reconstruct the object height using only two
312 linear-coded triangular intensity patterns [67]. However, as triangular patterns are characterized
313 by sharp corners, their measurement precision is more sensitive to projector gamma non-linearity
314 and image defocus when compared to sinusoidal phase shifting techniques [68].

315 Finally, several sinusoidal phase shifting profilometry techniques have been reported that replace
316 one or two of the phase-shifted fringe patterns of a 3-or 4-step projection cycle with a uniformly
317 lit [69,70] or linearly increasing [71] intensity image or employ different fringe pattern
318 frequencies in each of the projected images [72]. The *2 + 1 modified sinusoidal* profilometry
319 technique [69,70] requires two sinusoidal fringe pattern projections with a relative phase shift of
320 $\pi/2$ and a third uniformly lit flat image of the measurement target to extract full-field depth
321 information. This specific modification makes the *2 + 1* technique more suitable to measure
322 moving targets, as the third, flat image is less sensitive to object motion between successive
323 frames. On the other hand, the decrease in deformed fringe patterns from 3 to 2 per measurement
324 cycle has a (slight) negative effect on the acquired measurement precision [73]. In addition, the
325 three obtained images are no longer interchangeable and the order in which the *2 + 1* fringe
326 patterns enter the digital signal processing pipeline becomes relevant. This requires additional
327 signal processing to detect the uniformly lit image in the sequence or custom timing
328 synchronization between projector and camera. Alternatively, the *2 + 2 modified sinusoidal*
329 profilometry technique [71] replaces the uniformly lit image of the measurement target with two

330 linearly increasing/decreasing intensity ramp patterns to reconstruct the object surface profile.
331 Although the requirement for an additional frame reduces the maximum obtainable 3D frame
332 rate, it permits the calculation of a *base phase* which facilitates the phase unwrapping process
333 and thereby significantly reduces the complexity of the reconstruction algorithm. Finally, phase
334 error reduction has been demonstrated in 3-step phase shifting profilometry when the fringe
335 pattern frequencies of successively projected images are chosen so that they obey certain general
336 rules that confine their relative sizes to specific base frequency ratios [72].

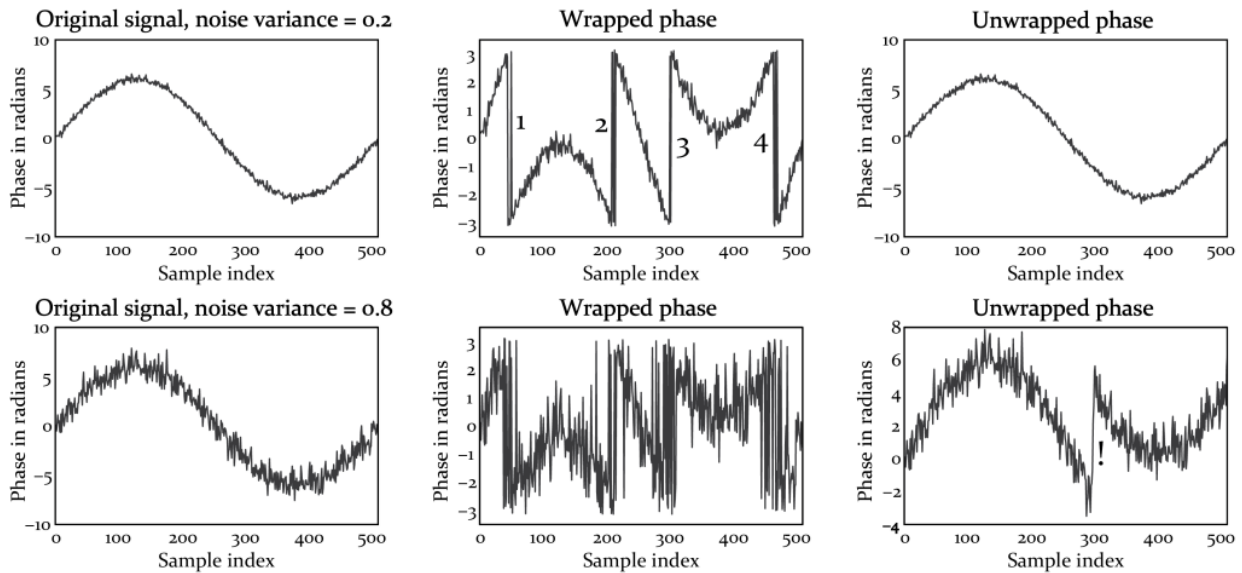
337 **2.5 Hybrid methods**

338 When measurement speed is not an issue, an object surface can be mapped by any successive
339 combination of structured light profilometry techniques in a single measurement. By selecting
340 complementary techniques, the respective strengths of different methods can be cumulated and a
341 higher quality 3D surface profile can be obtained. One of the most common combinations found
342 in industrial applications that employ structured light to map the surface of static objects is the
343 pairing of phase shifting techniques with binary or gray code profilometry [74,75]. The
344 robustness against measurement noise of binary techniques allows for a first, rudimental surface
345 map of the object to be formed of which the axial resolution can subsequently be improved using
346 a set of phase shifting techniques. This way, the phase unwrapping procedure can be avoided and
347 the 3D measurement becomes fully automated. Another way of avoiding the time-consuming
348 and error-prone process of phase unwrapping is by combining multiple sets of phase shifting
349 cycles in a dual- or multi-frequency pattern scheme. This can be achieved by either including one
350 or more additional cycles with large fringe pitches so that the entire measurement falls within a
351 single fringe plane [76], or by combining two or more sets of different fringe periods in the
352 creation of a virtual fringe pattern with a larger equivalent pitch [77,78]. In addition, when the
353 frequency ratio in multi-frequency pattern schemes is selected properly, non-linear phase errors
354 generated by the inevitable non-sinusoidality of discretely sampled fringe patterns can be
355 reduced [79]. Alternatively, composite fringe patterns have been constructed that contain both
356 low- and high-frequency components [80–82]. Subsequent Fourier analysis of the obtained
357 multi-frequency fringe patterns allows the reconstruction of the individual phase maps
358 corresponding to each input frequency, the calculation of a unit-frequency phase map and the
359 creation of phase partitions. Finally, Koninckx et al. [83–85] and Griesser et al. [86] have
360 reported an *adaptive structured light* technique which optimizes the nature, color and/or amount
361 of projected patterns in function of the object surface and measurement conditions. Depending
362 on the object, sparse color coding of the base stripe pattern, superimposition of unique code
363 points onto projected stripes or a combination is employed. Using a feedback loop, the projected
364 patterns can be self-adapting to render the technique more robust against scene variability.

365 **3. Phase unwrapping**

366 Many of the structured light profilometry techniques obtain phase information that is
367 mathematically constrained or ‘wrapped’ to its principal value domain. Typically, this
368 constriction occurs when the digital signal processing technique used in the reconstruction
369 algorithm employs an inverse- or arctangent function to retrieve the phase signal. Considering
370 the principal value domain of the (four-quadrant) arctangent function, such phase signals are
371 generally wrapped to the finite interval $[-\pi, \pi]$ and require custom digital signal processing

372 techniques to remove the artificial 2π -discontinuities or ‘phase jumps’ from the signal. The
 373 procedure of extracting the original continuous phase from the wrapped input phase signal is
 374 commonly referred to as ‘phase unwrapping’. It should be noted, though, that calculation of an
 375 arctangent function as part of the phase extraction algorithm is not an exclusive demand to
 376 require phase unwrapping. Structured light profilometry techniques which combine periodic
 377 fringe patterns with intensity ratio calculations generally also produce wrapped phase data,
 378 which can now be restricted to any finite interval, based on the projected intensity profiles and
 379 the employed reconstruction process. Nevertheless, whether the value of the phase jumps is 2π or
 380 any discrete number, the requirement for phase unwrapping stands and its basic principles
 381 remain valid.



382
 383 Figure 1: Graphical representation of the one-dimensional phase unwrapping process. Top row:
 384 sine wave with added Gaussian noise (variance set to 0.2). Bottom row: sine wave with added
 385 Gaussian noise (variance set to 0.8). Four phase jumps (denoted by the numerators 1-4) are
 386 present in the wrapped signal. Rising noise levels cause the phase unwrapping procedure to miss
 387 one of the four phase jumps in the wrapped phase signal, leading to a distortion artifact (denoted
 388 by the exclamation mark) that propagates throughout the remainder of the signal.

389 In one-dimensional signals, the phase unwrapping problem is reduced to the detection and
 390 subsequent removal of phase jumps by adding an integer multiple of 2π to each sample value so
 391 that the numerical difference between neighboring sampling points is everywhere less than π . In
 392 practice, one starts from the second sampling point from the left in the wrapped phase signal and
 393 calculates the difference between the current sample and the one directly adjacent to the left. If
 394 this difference is larger than π , subtract 2π from the current sample and from all samples to the
 395 right of it. If the difference is smaller than $-\pi$, add 2π to the current sample and to all samples
 396 to the right of it. Move on to the third sample from the left and repeat this process until the last
 397 sample in the signal is reached. A graphical representation of the one-dimensional phase
 398 unwrapping procedure is presented in Figure 3.

399 A sine wave of amplitude larger than π is simulated, the signal is distorted with additive
 400 Gaussian noise and wrapped to the finite interval $[-\pi, \pi]$ by calculating its four-quadrant

401 arctangent function. When noise levels remain sufficiently low, the phase unwrapping algorithm
402 is able to detect the four phase jumps that are present in the wrapped phase and correct for them
403 accordingly. However, when the signal suffers from higher noise levels or insufficiently dense
404 signal sampling, it can have catastrophic effects on the outcome of the phase unwrapping
405 procedure. This is illustrated in the bottom row of Figure 3 where increased noise levels have
406 caused the phase unwrapping algorithm to miss one of the four original phase jumps. Random
407 noise has reduced the difference between the sampling points on either side of the third
408 discontinuity to less than π and no phase jump is detected. Conversely, in addition to the miss of
409 genuine phase jumps, higher noise levels or undersampling of the phase signal may also lead to
410 the incorrect detection of ‘fake’ phase jumps, when the difference between adjacent continuous
411 sampling points has been erroneously increased to more than π . As the phase unwrapping
412 process is accumulative in nature, the resulting errors propagate throughout the remainder of the
413 signal. This principle makes the design of robust phase unwrapping algorithms so challenging.

414 In two-dimensional signals, the phase unwrapping problem becomes vastly more complex and
415 much more interesting. As phase jumps can occur both horizontally and vertically within the
416 phase map, each pixel (barred those at the borders) now has four nearest neighbors that require
417 discontinuity checking. In addition, the order in which pixels are unwrapped greatly determines
418 the final outcome of the algorithm. Since expansion of the phase unwrapping algorithm to two
419 dimensions does not void its accumulative nature, it is of crucial importance to avoid
420 unwrapping artifacts early on in the phase unwrapping procedure. To this end, the classical
421 approach to aid the two-dimensional phase unwrapping algorithm in selecting its optimal path of
422 integration is to provide it with a pre-calculated pixel quality map. This way, high-quality pixels
423 (or pixels with little local noise) can be unwrapped first and low-quality pixels (or pixels with
424 high local noise) can be unwrapped last, limiting the propagation of errors throughout the
425 unwrapped phase map. These processing schemes are commonly referred to as ‘quality guided’
426 phase unwrapping algorithms [87–89]. As a specific order of unwrapping is maintained and no
427 two unwrapping operations can take place at the same time, this particular approach to phase
428 unwrapping is inherently serial. In order to introduce some parallelism into two-dimensional
429 phase unwrapping and to increase its potential processing speed, a host of phase unwrapping
430 algorithms has been designed over the years that mainly provide varying compromises between
431 the classic trade-off between speed and accuracy. Examples of theoretical principles that have
432 been used to solve the two-dimensional phase unwrapping problem include the following: multi-
433 level or discrete quality maps [90,91], Bayesian approaches [92], Markov random fields [93],
434 region growing algorithms [94], neural networks [95], genetic algorithms [96], Green’s functions
435 [97], fractals [98], network flow algorithms [99], cellular automata [100], L_p -norm minimization
436 [101] and statistical approaches [102]. Detailed descriptions of these methods fall outside the
437 scope of the presented work, but it can be noted that what they all have in common is that the
438 overall quality of phase unwrapping generally improves with increased processing time. Note
439 also that the phase unwrapping problem can be expanded to 3 or even N dimensions. Although
440 multi-dimensional expansion increases the complexity of the problem, many of the core
441 principles upon which two-dimensional phase unwrapping algorithms are based can be
442 transferred to solve the problem in N dimensions [103,104].

443 As phase unwrapping is a crucial step in many structured light profilometry techniques, their
444 integration in digital processing pipelines is a common bottleneck in real-time applications that
445 require phase data to be unwrapped before visualization. At the time of writing, only two reports

446 have been made of phase unwrapping techniques that are able to operate in real-time setups.
 447 Zhang et al. [91] presented a multi-level approach with an optimized scan-line algorithm to
 448 process VGA resolution phase maps within 18.3 ms. Recently, we transferred the phase
 449 unwrapping problem to Fourier space and demonstrated <5 ms processing capability for VGA
 450 resolution phase data by using a graphics processing unit [105].

451 **4. Real-time structured light profilometry**

452 Though many structured light profilometry techniques have found their way into practical
 453 applications, only few of them are implemented in *real-time* setups. Table 1 provides a
 454 chronological overview of systems that have reported simultaneous acquisition, digital signal
 455 processing and display of full-field 3D surface maps in a continuous loop of at least 10 frames
 456 per second (fps). Although the threshold of 10 fps as qualification limit for a system to be ‘real-
 457 time’ is chosen somewhat arbitrarily, it does correspond to the speed limit at which the human
 458 visual system is found to be able to process and perceive different images individually [106].
 459 Furthermore, it should be noted that we have normalized the reported 3D frame rates of the
 460 various sequential projection techniques by reducing their respective frame rate in case identical
 461 fringe patterns are re-used in subsequent processing cycles. This allows for a more objective
 462 comparison of the so-called pseudo-real-time systems with systems that employ only newly
 463 acquired fringe patterns every 3D measurement. In the remainder of the section, we describe the
 464 main advances in digital projection technology and coding strategy that have led to the
 465 development of these real-time structured light profilometry systems.

Author	SLP technique	Year of publication	Projection technique	CCD (pixels)	3D frame rate (fps)
Hall-Holt et al. [53], Rusinkiewicz et al. [54]	Stripe boundary code	2001, 2002	DLP	640 x 240	15
Huang et al. [107]	3-step sinusoidal	2003	DLP	640 x 480	16
Koninckx et al. [83–85], Griesser et al. [86]	Adaptive structured light	2003, 2004, 2006	LCD	640 x 480	10-25*
Zhang et al. [66,108]	3-step trapezoidal	2004, 2006	DLP	532 x 500	40
Pan et al. [109]	N-ary gray code	2004	DLP	640 x 480	40
Zhang et al. [69,110]	2 + 1 sinusoidal	2006, 2007	DLP	640 x 480	60
Liu et al. [111]	5-step dual frequency sinusoidal	2010	DLP-evaluation module	640 x 480	20
Zuo et al. [71]	2 + 2 sinusoidal	2012	DLP	640 x 480	30
Karpinsky et al. [78]	6-step dual frequency 3-step sinusoidal	2014	DLP-evaluation module	800 x 600	30
Van der Jeught et al. [112]	4-step sinusoidal	2015	DLP-evaluation	640 x 480	30

			module		
Nguyen et al. [113]	3-step sinusoidal	2015	DLP	640 x 480	45

466 * Exact frame rate depends on scene complexity

467 Table 1: Chronological overview of publications that have reported real-time acquisition,
468 processing and displaying of 3D surface maps.

469 **4.1 Digital fringe pattern projection**

470 As previously stated, the advent of low-cost digital projection hardware has been instrumental to
471 the development of real-time structured light profilometry techniques. One of the first systems to
472 employ a digital video projector as a means to quickly shift between successive fringe pattern
473 images in a multi-shot profilometry technique was presented by Hall-Holt et al. [53] and
474 Rusinkiewicz et al. [54]. By projecting a four-frame sequence of binary fringe patterns onto the
475 measurement target at a rate of 60 Hz, a unique surface map could be extracted from the
476 deformed fringe patterns 15 times per second. By tracking the boundaries between black and
477 white fringes between successive fringe projections, the system was able to correct for slow in-
478 plane object motion (of between one-fourth and one-half stripe-width per frame) within a single
479 measurement cycle. Whereas previous implementations of the *stripe boundary code*-based
480 pipeline required human intervention at various stages of the 3D measurement process [114,115],
481 digitalization and synchronization of the projector-camera system increased the level of
482 automation, permitted the user to rotate the measurement target by hand and see a continuously-
483 updated model as the object was scanned. This both increased user interaction and allowed for
484 the construction of complete 3D surface models of the measurement target to be reconstructed at
485 reasonably high speeds.

486 Similarly, the real-time adaptive structured light systems presented by Koninckx et al. [83–85]
487 and Griesser et al. [86] employed fast digital projection hardware to modify the projected fringe
488 patterns on-line. In contrast to other structured light profilometry techniques which employ static
489 code patterns that are supposed to work under all circumstances, the digital signal processing
490 speed of adaptive light techniques is dependent on the object properties and can therefore lead to
491 varying 3D frame rates. By adapting the fringe pattern pitch, code line position and color
492 markers in function of the texture and reflective properties of the object surface, measurement
493 precision and system robustness could be increased. This online feedback-loop was controlled in
494 system memory and was maintained in real-time by utilizing the high data transfer rate between
495 the graphics card and the digital projector.

496 **4.2 DLP modifications and digital micromirror devices**

497 Ultimately, the speed of sequential or adaptive structured light profilometry techniques is limited
498 by the transfer rate between graphics card and projector. At the time of writing, the maximum
499 speed at which consumer-grade digital projection systems can switch between unique input
500 frames is limited to 60 frames per second [73]. This means that if a digital projector cycles
501 through sets of 3-or 4-step fringe patterns in a continuous loop, the maximum obtainable 3D
502 frame rate of the corresponding profilometry system is limited to 20 fps or 15 fps, respectively.
503 To this end, Huang et al. [107] modified a DLP to project three phase-shifted, sinusoidal fringe
504 patterns at a switching speed of 300 Hz. DLP's typically contain a 2D array of digital
505 micromirror devices (DMD's) which rotate over an angle at high speeds to reflect light either

506 towards or away from the objective lens. This way, the intensity of every pixel in the formed
507 image can be controlled individually. The red, green and blue (and sometimes cyan, magenta,
508 yellow and/or white) color components of an image are separated by the DLP on-chip and are
509 projected successively at high speeds by synchronizing the digital micromirror state with the
510 position of a rapidly rotating color wheel. The high switching speed allows the projected color
511 sequence to be interpreted by the human brain as a single full-color image. Huang et al.
512 combined three phase-shifted sinusoidal fringe patterns into a single static RGB-color image that
513 was projected by the DLP. By removing the color wheel of the projector and synchronizing the
514 DLP-camera system, grayscale phase shifted images could be captured at a maximum speed of
515 300 Hz. The employed 85 fps camera was only able to capture a single phase-shifted fringe
516 pattern every two projection cycles, however, resulting in an actual 3D measurement speed of 16
517 fps. Nevertheless, the principle of color separation in modified DLP's was demonstrated and the
518 potential speed of multi-shot profilometry techniques was increased. Later, the same DLP-
519 modification was used by Zhang et al. in a system with a 240 Hz DLP and a 262 fps camera
520 [66,108]. Here, a full three-step pattern sequence was captured within two projection cycles,
521 leading to a 3D measurement speed of 40 fps. Because the arctangent-function required in the
522 digital signal processing pipeline to retrieve the phase map proved to be too time-consuming for
523 real-time applications, a new intensity ratio technique was employed. Similar to trapezoidal
524 phase shifting profilometry, the phase was determined from direct intensity ratio calculations of
525 the captured intensity profiles. Instead of fringe patterns with trapezoidal intensity profiles,
526 regular sinusoidal fringe patterns were projected and a look-up-table was constructed to correct
527 for the systematic measurement errors in the intensity ratio map induced by the non-linearity of
528 the fringe patterns. The entire digital signal processing pipeline, including a custom spatial phase
529 unwrapping algorithm, was able to follow the camera's rate of acquisition and resulted in the
530 reconstruction of 40 height maps per second.

531 Pan et al. employed the same setup as Huang and Zhang in a 3-step N-ary gray code system
532 [109]. Here, the intensity values of all pixels in the 3 acquired images are digitized into N
533 different levels (Pan implemented ternary $N = 3$ and sextanary $N = 6$ code patterns) and code
534 words are determined along the decoding direction for each pixel at a rate of 40 fps. Since the
535 authors define these code words periodically to increase lateral resolution, a process similar to
536 phase unwrapping is required to extract the continuous phase map from the sawtooth-like phase
537 profile. In general, N-ary gray code profilometry is more robust to random noise than phase
538 shifting techniques that employ the same amount of fringe images, but has lower measurement
539 accuracy since a smaller range of discretized intensity values are used to reconstruct the height
540 map.

541 Later, Zhang et al. reduced motion errors by replacing the 3-step phase shifting profilometry
542 technique with a 2+1 technique that requires two π -shifted fringe patterns and a uniformly lit
543 image of the object [64,100]. After detection of the flat image, the three images are combined
544 into a single 3D measurement. The main advantage of this technique is the fact that every third
545 image of the projected cycle is now unimpeded by object motion, making it less sensitive to
546 movement of the measurement target between successive frames. Additionally, inclusion of a flat
547 image in the measurement cycle allows for direct texture acquisition of the object surface which
548 is an important asset in applications such as face recognition, computer vision, computer
549 graphics, etc. Meanwhile, a higher-speed 180 fps camera was used in the experimental setup and
550 a 3D frame rate of 60 fps was obtained. Other reports of real-time setups that employ modified

551 consumer-grade DLP's include implementations of 2+2 sinusoidal profilometry [71] and 3-step
552 sinusoidal profilometry [113].

553 More recently, compact DMD discovery boards became available that contain a digital
554 micromirror device with on-board flash memory for pattern storage
555 (<http://www.ti.com/tool/dplightcrafter>). Though the light source and the projection optics on
556 these modules are basic, they provide access to the DMD controller board and allow the user to
557 cycle through predefined 8-bit patterns at a rate of up to 120 Hz and through binary patterns at a
558 rate of up to 4000 Hz. In addition, these evaluation modules provide configurable I/O triggers for
559 synchronization with cameras, sensors, etc. Liu et al. were the first to implement a Texas
560 Instruments Discovery 1100 board in their real-time setup as projection engine to a dual
561 frequency projection scheme [111]. Moving hand gestures were scanned using 6 patterns per 3D
562 measurement, yielding a 3D frame rate of 20 fps. Later, Karpinsky et al. increased this frame rate
563 to 30 fps by synchronizing the binary projection mode of a Texas Instruments Lightcrafter board
564 with a 180 Hz camera [78]. Recently, we used the Lightcrafter board to inject structured light
565 patterns into one of two optical pathways of a surgical stereomicroscope. After synchronization
566 with a high-speed camera that was placed in the second optical pathway, we were able to
567 acquire, process and display 30 microscopic height maps per second using standard 4-step
568 sinusoidal phase shifting profilometry. This allowed the qualitative depth perception of the
569 stereomicroscope operator to be enhanced by live quantitative height measurements with depth
570 resolutions in the micrometer range [112].

571 **4.3 Dual frequency projection to avoid phase unwrapping**

572 Robust spatial phase unwrapping algorithms are generally computationally intensive and their
573 design typically requires multiple iterations to reach convergence, leading to high execution
574 times. Very basic phase unwrapping techniques such as flood-fill and scan-line algorithms have
575 been reported to work in real-time [108], but they are very sensitive to noise and often generate
576 artifacts that significantly reduce the quality of the height map. The multi-level phase
577 unwrapping algorithm designed by Zhang et al. [91] combines the speed of scan-line algorithms
578 with the robustness of multi-level techniques. However, it still relies on entirely continuous and
579 connected phase maps as input, making the profilometry system unsuitable for measurements of
580 objects containing isolated regions or phase discontinuities greater than one period. To this end,
581 multi-frequency techniques have been employed in real-time setups to avoid spatial phase
582 unwrapping, at the cost of an increased number of fringe patterns per projection cycle. Liu et al.
583 [111] propose a 5-pattern dual-frequency pattern scheme that combines a high-frequency
584 component with a low-frequency component into a single fringe pattern. The high-frequency
585 component generates a high-resolution wrapped phase map while the low-frequency component
586 provides a base phase map that can be used to guide the phase unwrapping procedure of the
587 high-frequency map. Alternatively, Zuo et al. [71] propose a four-pattern algorithm containing
588 two π -shifted fringe planes and two linearly increasing/decreasing intensity planes to construct
589 the base phase map. Finally, Karpinsky et al. [78] adopt a two-frequency 6-step phase shifting
590 algorithm with different fringe pitches. These fringe pitches P_1 and P_2 are combined into a virtual
591 fringe pattern with an *equivalent* fringe pitch of $P_1 P_2 / |P_1 - P_2|$. By properly selecting the spatial
592 frequencies of the dual-frequency patterns, an equivalent phase map can be constructed that
593 spans the entire image without 2π -discontinuities.

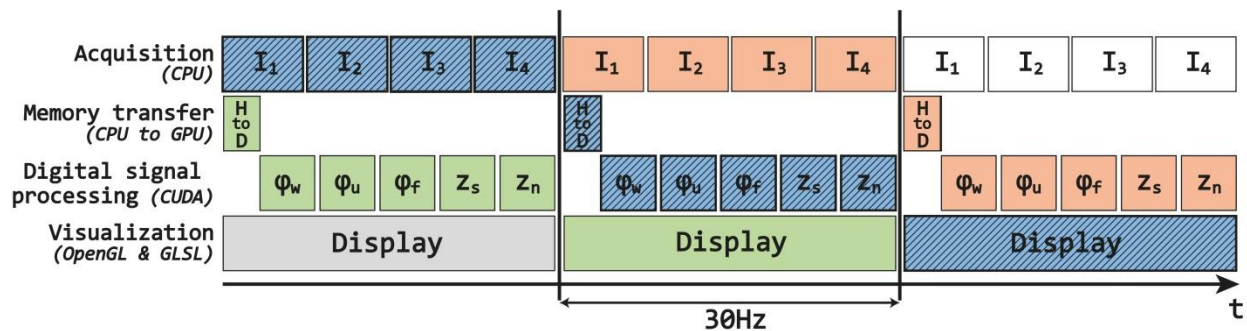
594 The major advantage of multi-frequency projection techniques is the fact that the problem of
595 phase unwrapping is reduced to the calculation of an additional phase map, after which a simple
596 pixel by pixel subtraction and rounding operator suffices to reconstruct the absolute phase map.
597 Second, having a low-frequency base phase allows for the measurement of multiple, non-
598 connected objects or allows the imaged object to contain isolated patches. Finally, all of these
599 calculations can be done concurrently on all pixels, making the technique highly suitable for
600 parallel implementation. Besides the obvious disadvantage of requiring additional images, multi-
601 frequency techniques contain projection cycles of which the fringe patterns are no longer
602 interchangeable. In contrast to regular 3-or 4-step phase shifting profilometry, the order in which
603 the fringe patterns are recorded is relevant to the reconstruction algorithm. This requires either
604 additional digital signal processing to detect the various projected patterns or custom triggering
605 between DLP and camera to mark the beginning of each measurement cycle.

606 **4.4 GPU's and parallel processing pipelines**

607 As the frame rate of structured light profilometry techniques increases, the amount of processing
608 power required to reconstruct and visualize the 3D surface profile increases as well. In the early
609 days of real-time phase shifting profilometry, direct calculation of the arctangent function (e.g.
610 atan2 in C++) proved to be too slow to extract the phase from sinusoidal fringe patterns in real-
611 time applications. In order to avoid this computational bottleneck, Zhang et al. developed a
612 whole new phase shifting profilometry technique involving trapezoidal intensity profiles and
613 look-up-tables to approximate the arctangent function [66,108]. Meanwhile, processing hardware
614 has evolved in such a way that arctangent calculations can be calculated efficiently at reasonably
615 high speeds, allowing the direct extraction of phase maps in real-time systems [78,112]. An
616 important factor in this evolution is the increase in processing power of multicore parallel
617 hardware over the last decade and the development of general-purpose graphics processing unit
618 (GPGPU) programming [116]. Graphics processing units are specialized co-processors to the
619 central processing unit (CPU) that were initially designed to perform graphics rendering tasks.
620 Because of their recent increase in processing power, modern GPU's are commonly adopted in
621 high-performance computing setups in scientific, engineering, analytics and consumer
622 applications. GPU's typically contain a large number of streaming processors that operate
623 concurrently and therefore require a custom parallel programming approach. In general, phase
624 shifting profilometry techniques are highly suitable for parallel implementation as the phase
625 value at each pixel coordinate can be calculated independently from those at neighboring pixels.

626 Zhang et al. reported a 4× increase in processing speed using a Quadro FX 3450 GPU over a
627 dual 3.4Ghz CPU workstation in their real-time 2+1 phase shifting profilometry system [69].
628 Karpinsky et al. employed a Quadro NVS5400M GPU in their dual-frequency system to enable
629 phase wrapping, base phase unwrapping, Gaussian filtering, normal calculation and 3D rendering
630 at a frame rate of 30 Hz [78]. Recently, we developed a real-time noise-resistant spatial phase
631 unwrapping algorithm by transferring the periodic phase unwrapping problem to Fourier space
632 and by optimizing it for implementation on parallel hardware [105]. We have demonstrated its
633 real-time capabilities (< 5 ms for a 640 × 480 pixel phase map) and robustness to image noise on
634 phase maps that were gathered with regular 4-step sinusoidal phase shifting profilometry, both in
635 real-time macroscopic [105] and microscopic [112] setups.

636 One of the major bottlenecks in GPGPU programming is caused by the limited bandwidth of the
637 PCI bus across which data between host (CPU) memory and device (GPU) memory is
638 transferred. In order to hide this latency, the real-time profilometry pipeline needs to be
639 organized in such a way that its architecture enables maximum concurrency of acquisition,
640 memory transfer, digital signal processing and visualization. In Fig. 4, we present a schematic
641 overview of such a pipeline that is optimized for real-time 4-step phase shifting profilometry
642 [112]. At all times, fringe pattern acquisition, digital signal processing, and on-screen rendering
643 of successive measurements are executed in parallel. Following the data processing cycle of one
644 3D measurement (blue, diagonally hatched), four input fringe patterns $I_1 - I_4$ are captured by the
645 high-speed camera every 33.33 ms and are transferred from CPU to GPU memory. Next, the
646 digital signal processing pipeline performs successive wrapped phase extraction (φ_w), phase
647 unwrapping (φ_u), Gaussian filtering (φ_f), phase-to-height conversion and scaling (z_s), and
648 normal calculation (Z_n). Finally, the height and normal maps are combined to render the 3D
649 height measurement. It should be noted that the digital signal processing and memory transfer
650 blocks as illustrated in Fig. 4 are not scaled to represent the respective time they take, but are in
651 fact expanded to fill the maximum time slot they could take up without obstructing the real-time
652 pipeline. In reality, the entire digital signal processing scheme, including memory transfer from
653 host to device, takes up only 16.3 ms in total on a workstation containing a GTX770 graphics
654 card and a dual core Intel i5 processor.



655
656 Figure 4: (color online) Schematic overview of a real-time 4-step phase shifting profilometry
657 pipeline. Horizontally aligned blocks occur sequentially; vertically aligned blocks occur
658 simultaneously.

659 4.5 Binary defocus and ultra-fast 3D measurement speed

660 Although a 3D frame rate of 30-60 fps is sufficiently fast to capture slow object motion, higher
661 speeds may be necessary if one wants to measure faster moving objects such as, for example,
662 beating hearts, vibrating membranes or rotating fan blades. The most important feature of such
663 ultrahigh-speed setups is not to process the acquired phase maps in real-time (the effect of
664 adding more frames per second beyond 30 becomes negligible to human perception anyway) but
665 to shorten the acquisition window so that the effect of motion artifacts may be reduced. In this
666 regard, a sensible strategy would be to employ single-shot structured light profilometry
667 techniques, since in that case a static fringe pattern may be projected and the 3D frame rate is
668 limited only by the acquisition speed of the camera. Although pre-designed mechanical gratings
669 or custom patterns may be used in combination with a continuous light source to illuminate the
670 object with a static fringe pattern, they lack the flexibility of digital projection hardware.

671 To this end, Gong et al. reported the use of an off-the-shelf DLP projector in combination with
672 standard Fourier transform profilometry to reach a 3D rate of 4000 Hz [117]. Instead of
673 projecting a static 8-bit pattern onto the object, which would limit the pattern projection rate to
674 the refresh rate of the DLP device, a static binary pattern (each pixel set to either 0 or 255) was
675 used. Due to the fundamental image generation mechanism of DMD's, this resulted in the
676 micromirrors being fixed in either the ON or OFF position 100% of the time. Since DLP's
677 employ a continuous LED/Laser lamp light source, customizable binary digital fringe patterns
678 can be projected in a static loop without glitches. Gong et al. realized that the binary nature of the
679 produced fringe patterns was less than ideal for the application of Fourier transform
680 profilometry, so they applied the *binary defocusing* technique proposed by Su et al. [118] and
681 Lei et al. [119]. By deliberately defocusing the binary patterns, sinusoidal fringe patterns can be
682 approximated at the cost of reduced contrast.

683 Alternatively, the binary projection mode of DLP evaluation modules allows projection of binary
684 fringe patterns at display rates of 4000-10000 Hz, depending on the controller board model and
685 pixel resolution. Takei et al. [120], Zhang et al. [121], Wang et al. [77] and Zuo et al. [122]
686 employed different models of the TI Discovery board in ultrahigh-speed profilometry systems
687 based on various combinations of binary code and sinusoidal phase shifting profilometry.
688 Sinusoidal fringe patterns were obtained through regular binary defocusing [121] or by
689 modifying the binary patterns according to the *optimal pulse width modulation* technique
690 [77,122]. This technique selectively eliminates undesired frequency components by inserting
691 different types of notches into a conventional binary square wave in order to generate higher-
692 quality sinusoidal fringe patterns. These systems enabled 3D acquisition rates in the order of
693 hundreds to thousands of full-field height measurements, depending on the technique and the
694 employed camera.

695 **5. Discussion**

696 **5.1 Single-shot versus multi-shot techniques**

697 Although single-shot structured light profilometry techniques have inherent speed advantages
698 over multi-shot techniques, there are only a few reports of them being used in real-time systems
699 [83–86]. The relative underrepresentation of single-shot techniques in real-time 3D surface
700 measurement applications may be due to the fact that extensive digital signal processing is
701 required to extract high-quality full-field height maps from a single frame. For example, if one
702 wants to automate the otherwise manual procedure of fundamental frequency selection in Fourier
703 transform profilometry, additional data operations such as window filtering or empirical mode
704 decomposition are necessary. Even when implemented on parallel hardware, windowed FTP
705 techniques have been reported to be limited to 4 frames per second for maps of 256×256 pixels
706 [123]. Furthermore, the measurement accuracy of single-shot techniques is generally determined
707 by the uniform, color-independent reflection profile of the measurement target surface [124]. To
708 reduce the effect of cross-talk between different color channels and thereby to minimize its
709 adverse effect on axial resolution, extra color decoupling calculations are required.
710 Unfortunately, these algorithms are known to be very time-consuming [125,126]. In addition,
711 most measurement targets in structured light profilometry applications contain non-uniform
712 surface reflectivity profiles. Poor local reflection causes fringe pattern contrast to diminish and

713 measurement accuracy to drop. In general, single-shot techniques are more sensitive to such
714 contrast variations than multi-shot techniques since they are unable to assess the local reflectivity
715 in function of the projected intensity level. Multi-shot techniques, on the other hand, do have the
716 opportunity to account for non-uniform reflectivity profiles by incorporating intensity-ratio
717 calculations in their height extraction algorithms. By dividing successive frames that have been
718 illuminated with different intensity levels on a pixel-per-pixel basis, local reflectivity is
719 normalized and measurement accuracy increased. This explains why the majority of reported
720 real-time SLP techniques that have been used in practical applications are based on multi-shot
721 intensity-ratio algorithms.

722 **5.2 Challenges**

723 It seems that the main challenges facing real-time surface measurement systems are threefold:
724 first, fringe projection speed is currently the limiting factor in the frame rate of 3D structured
725 light profilometry systems. In order to increase maximum potential imaging speed, projection
726 hardware technologies need to improve. Second, structured light profilometry systems are rather
727 large in size and weight and should be miniaturized to become implementable in practical
728 medical or consumer-grade applications. Third, digital signal processing pipelines need to be
729 able to keep up with the increasing rate of fringe plane acquisition. To this end, the design of
730 parallel pipelines and the optimization of height extraction kernels to run on parallel hardware
731 could become increasingly important.

732 Currently, the fastest 3D shape measurement systems [69,110] are able to produce 60 height
733 maps per second, which is still not fast enough for many real-time applications. In order to
734 measure fast-moving object surfaces such as beating hearts, rapidly speaking human face
735 contours or rotating fans in real-time, imaging speeds of up to 300-400 3D frames/sec might be
736 mandatory [73]. These speeds may be obtainable by using the binary defocusing technique in
737 combination with DLP evaluation modules, but here axial resolution is sacrificed in favor of
738 speed. If one wants to maintain true 8-bit grayscale projection of fringe patterns, DMD switching
739 speed needs to increase. As there is no incentive for off-the-shelf projector manufacturers to
740 increase DLP frame rate (as these are already above the maximum input signal refresh rate and
741 the speed threshold for human sight already), advancements in this area are to be expected to
742 come from DLP evaluation modules that are designed specifically for this purpose.

743 Projection hardware is also generally the largest component in real-time structured light
744 profilometry systems. CCD-based cameras and lens optics are rather small and portable laptop
745 computers have been shown to provide sufficient computational power to support real-time
746 pipelines [78] but typical projection hardware is comparatively large and heavy. Conventionally,
747 halogen lamps are used in commercial LCD or DLP projectors. These lamps generate a large
748 amount of heat and require extensive cooling mechanisms. Recently, halogen lamps have been
749 replaced with LED lamps in projection hardware developed by multiple companies including
750 Mitsubishi, Samsung, Dell, Lg and Hitachi [73]. These lamps can be made much smaller and
751 typically generate less heat, which has led to their incorporation into smaller DLP evaluation
752 modules. Although these modules do allow more compact and portable 3D surface shape
753 measurement systems to be assembled [78,112], the resulting projector-camera systems might
754 need additional miniaturization to become practical in handheld 3D scanning applications.
755 Furthermore, evaluation module light source power emission is still too low (typically several

756 tens to several hundreds of lumen) to produce high-quality results in suboptimal lighting
757 conditions.

758 Simultaneous acquisition, digital signal processing and displaying of surface maps in a triple-
759 buffer strategy (Figure 4) is a good way to distribute the workload across multiple co-processors
760 as it enables thread concurrency and reduces system latency. Parallel processing pipelines ensure
761 that height extraction and possible phase unwrapping kernels get allotted the maximum amount
762 of processing time available. These time slots are ultimately limited by the total acquisition time
763 of the full fringe plane acquisition cycle, which, depending on the required amount of fringe
764 planes per measurement cycle, falls within the order of tens of milliseconds in high-speed
765 systems. Therefore, real-time structured light profilometry systems require optimized kernel
766 design and specialized parallel hardware such as graphics cards to follow the rate of acquisition.
767 Although the clock speed and number of multi-processors on graphics cards increases with each
768 new generation, it has been demonstrated that the largest bottleneck in GPU-based applications is
769 caused by the memory transfers between host and device memory [116]. As each new set of
770 input fringe data needs to be moved from host to device, structured light profilometry techniques
771 are heavily dependent on PCI-bus bandwidth. Currently, PCI-E bus bandwidth is limited to 5
772 GB/s at peak performance if optimal data transfer sizes are chosen and pinned memory is used.
773 As real-time SLP systems require the transfer of many small data blocks, memory transfer speed
774 can be up to an order of magnitude lower, on average [112]. Unless multiple fringe cycles are
775 bundled in a single data transfer and a slight lag is allowed, a memory transfer penalty of several
776 milliseconds per measurement is to be expected. Ideally, the PCI bus should be bypassed
777 altogether by enabling the CCD camera to offload image buffers directly into GPU memory, but
778 at the time of writing this feature is not supported by current hardware.

779 **6. Conclusion**

780 The last decade has witnessed a tremendous advance in the development of real-time structured
781 light profilometry setups, both in terms of speed and of quality. Technological improvements in
782 digital projection hardware and optimization of coding strategy have resulted in the production
783 of several optical profilometry systems that are able to produce high-quality three-dimensional
784 surface maps of dynamically moving targets at a refresh rate of several tens of frames per
785 second. In this paper, we have presented the underlying principles that allow these surface
786 mapping systems to operate in real-time and have discussed the remaining challenges that need
787 to be tackled towards further improvement.

788 **Acknowledgments**

789 Sam Van der Jeught acknowledges the support of the Research Foundation - Flanders (FWO).

790 **References**

- 791 [1] Ringbeck T, Hagebeuker B. A 3D time of flight camera for object detection. *Opt. 3D*
792 *Meas. Tech.*, 2007, p. 1–10. doi:10.1038/sj.jcbfm.9600416.
- 793 [2] Lange R, Seitz P. Solid-state time-of-flight range camera. *IEEE J Quantum Electron*

- 794 2001;37:390–7. doi:10.1109/3.910448.
- 795 [3] Hsu S, Acharya S, Rafii A, New R. Performance of a time-of-flight range camera for
796 intelligent vehicle safety applications. *Adv. Microsystems Automot. Appl.* 2006, 2006, p.
797 205–19. doi:10.1007/3-540-33410-6_16.
- 798 [4] Zhang RZR, Tsai P-STP-S, Cryer JE, Shah M. Shape-from-shading: a survey. *IEEE Trans*
799 *Pattern Anal Mach Intell* 1999;21. doi:10.1109/34.784284.
- 800 [5] Brooks MJ, Horn BKP. Shape and Source from Shading. *Shape from Shading* 1989:53–
801 68.
- 802 [6] Nayar SK, Nakagawa Y. Shape from focus. *IEEE Trans Pattern Anal Mach Intell*
803 1994;16:824–31. doi:10.1109/34.308479.
- 804 [7] Torreão JRA, Fernandes JL. Single-image shape from defocus. *Brazilian Symp. Comput.*
805 *Graph. Image Process.*, vol. 2005, 2005, p. 241–6. doi:10.1109/SIBGRAPI.2005.47.
- 806 [8] Brown MZ, Burschka D, Hager GD. Advances in computational stereo. *IEEE Trans*
807 *Pattern Anal Mach Intell* 2003;25:993–1008. doi:10.1109/TPAMI.2003.1217603.
- 808 [9] Scharstein D, Szeliski R. A taxonomy and evaluation of dense two-frame stereo
809 correspondence algorithms. *Int J Comput Vis* 2002;47:7–42.
810 doi:10.1023/A:1014573219977.
- 811 [10] Meadows DM, Johnson WO, Allen JB. Generation of surface contours by moiré patterns.
812 *Appl Opt* 1970;9:942–7. doi:10.1364/AO.9.000942.
- 813 [11] Chiang C. Moiré topography. *Appl Opt* 1975;14:177–9. doi:10.1364/AO.14.000177.
- 814 [12] Sansoni G, Biancardi L, Minoni U, Docchio F. Novel, adaptive system for 3-D optical
815 profilometry using a liquid crystal light projector. *IEEE Trans Instrum Meas*
816 1994;43:558–66. doi:10.1109/19.310169.
- 817 [13] Geng J. Structured-light 3D surface imaging: a tutorial. *Adv Opt Photonics* 2011;3:128.
818 doi:10.1364/AOP.3.000128.
- 819 [14] Geng J. Rainbow three-dimensional camera: new concept of high-speed three-dimensional
820 vision systems. *Opt Eng* 1996;35:376–83.
- 821 [15] Weinberg SM, Scott NM, Neiswanger K, Brandon CA, Marazita ML. Digital three-
822 dimensional photogrammetry: Evaluation of anthropometric precision and accuracy using
823 a Genex 3D camera system. *Cleft Palate-Craniofacial J* 2004;41:507–18. doi:10.1597/03-
824 066.1.
- 825 [16] Liu W, Wang Z, Mu G, Fang Z. Color-coded projection grating method for shape
826 measurement with a single exposure. *Appl Opt* 2000;39:3504–8.
- 827 [17] MacWilliams FJ, Sloane NJA. Pseudo-random sequences and arrays. *Proc IEEE*
828 1976;64:1715–29. doi:10.1109/PROC.1976.10411.
- 829 [18] Zhang LZL, Curless B, Seitz SM. Rapid shape acquisition using color structured light and
830 multi-pass dynamic programming. *Proceedings First Int Symp 3D Data Process Vis*
831 *Transm* 2002. doi:10.1109/TDPVT.2002.1024035.
- 832 [19] Zhang Z, Towers CE, Towers DP. Time efficient color fringe projection system for 3D
833 shape and color using optimum 3-frequency Selection. *Opt Express* 2006;14:6444–55.

- 834 doi:10.1364/OE.14.006444.
- 835 [20] Zhou C, Liu T, Si S, Xu J, Liu Y, Lei Z. An improved stair phase encoding method for
836 absolute phase retrieval. *Opt Lasers Eng* 2015;66:269–78.
837 doi:10.1016/j.optlaseng.2014.09.011.
- 838 [21] Boyer KL, Kak AC. Color-encoded structured light for rapid active ranging. *IEEE Trans*
839 *Pattern Anal Mach Intell* 1987;9:14–28. doi:10.1109/TPAMI.1987.4767869.
- 840 [22] Fernandez S, Salvi J, Pribanic T. Absolute phase mapping for one-shot dense pattern
841 projection. 2010 IEEE Comput. Soc. Conf. Comput. Vis. Pattern Recognit. - Work.
842 CVPRW 2010, 2010, p. 64–71. doi:10.1109/CVPRW.2010.5543483.
- 843 [23] Petriu EM, Sakr Z, Spoelder HJW, Moica A. Object recognition using pseudo-random
844 color encoded structuredlight. *Proc 17th IEEE Instrum Meas Technol Conf [Cat No*
845 *00CH37066]* 2000;3. doi:10.1109/IMTC.2000.848675.
- 846 [24] Salvi J, Pagès J, Batlle J. Pattern codification strategies in structured light systems. *Pattern*
847 *Recognit* 2004;37:827–49. doi:10.1016/j.patcog.2003.10.002.
- 848 [25] Payeur P, Desjardins D. Structured light stereoscopic imaging with dynamic pseudo-
849 random patterns. *Lect. Notes Comput. Sci. (including Subser. Lect. Notes Artif. Intell.*
850 *Lect. Notes Bioinformatics)*, vol. 5627 LNCS, 2009, p. 687–96. doi:10.1007/978-3-642-
851 02611-9_68.
- 852 [26] Desjardins D, Payeur P. Dense stereo range sensing with marching pseudo-random
853 patterns. *Proc. - Fourth Can. Conf. Comput. Robot Vision, CRV 2007, 2007*, p. 216–23.
854 doi:10.1109/CRV.2007.22.
- 855 [27] Le Moigne JJ, Waxman AM. Structured light patterns for robot mobility. *IEEE J Robot*
856 *Autom* 1988;4:541–8. doi:10.1109/56.20439.
- 857 [28] Griffin PM, Narasimhan LS, Yee SR. Generation of uniquely encoded light patterns for
858 range data acquisition. *Pattern Recognit* 1992;25:609–16. doi:10.1016/0031-
859 3203(92)90078-W.
- 860 [29] Maruyama M, Abe S. Range sensing by projecting multiple slits with random cuts. *IEEE*
861 *Trans Pattern Anal Mach Intell* 1993;15:647–51. doi:10.1109/34.216735.
- 862 [30] Durdle NG, Thayyoor J, Raso VJ. An improved structured light technique for surface
863 reconstructionof the human trunk. *Conf Proceedings IEEE Can Conf Electr Comput Eng*
864 *(Cat No98TH8341)* 1998;2. doi:10.1109/CCECE.1998.685637.
- 865 [31] Chen W, Su X, Cao Y, Zhang Q, Xiang L. Method for eliminating zero spectrum in
866 Fourier transform profilometry. *Opt Lasers Eng* 2005;43:1267–76.
867 doi:10.1016/j.optlaseng.2004.12.002.
- 868 [32] Li S, Su X, Chen W, Xiang L. Eliminating the zero spectrum in Fourier transform
869 profilometry using empirical mode decomposition. *J Opt Soc Am A Opt Image Sci Vis*
870 2009;26:1195–201. doi:10.1364/JOSAA.26.001195.
- 871 [33] Takeda M, Mutoh K. Fourier transform profilometry for the automatic measurement of 3-
872 D object shapes. *Appl Opt* 1983;22:3977. doi:10.1364/AO.22.003977.
- 873 [34] Hong G, Huang P. 3-D shape measurement by use of a modified Fourier transform
874 method. *Proc SPIE* 2008;7066:70660E.

- 875 [35] Li J, Su X-. Y, Gou L-. R. An improved Fourier transform profilometry for automatic
876 measurement of 3-D object shapes. *Opt Eng* 1990;29:1439–44.
- 877 [36] Lin JF, Su X-. Y. Two-dimensional Fourier transform profilometry for the automatic
878 measurement of three-dimensional object shapes. *Opt Eng* 1995;34:3297–302.
- 879 [37] Su X, Chen W. Fourier transform profilometry: A review. *Opt Lasers Eng* 2001;35:263–
880 84. doi:10.1016/S0143-8166(01)00023-9.
- 881 [38] Berryman F, Pynsent P, Cubillo J. The effect of windowing in Fourier transform
882 profilometry applied to noisy images. *Opt Lasers Eng* 2004;41:815–25.
883 doi:10.1016/S0143-8166(03)00061-7.
- 884 [39] Kemao Q. Windowed Fourier transform for fringe pattern analysis. *Appl Opt*
885 2004;43:2695–702. doi:10.1364/AO.43.002695.
- 886 [40] Huang L, Kemao Q, Pan B, Asundi AK. Comparison of Fourier transform, windowed
887 Fourier transform, and wavelet transform methods for phase extraction from a single
888 fringe pattern in fringe projection profilometry. *Opt Lasers Eng* 2010;48:141–8.
889 doi:10.1016/j.optlaseng.2009.04.003.
- 890 [41] Zhong J, Weng J. Spatial carrier-fringe pattern analysis by means of wavelet transform:
891 wavelet transform profilometry. *Appl Opt* 2004;43:4993–8. doi:10.1364/AO.43.004993.
- 892 [42] Li H, Yang C. Two-dimensional multiscale windowed Fourier transform based on two-
893 dimensional wavelet transform for fringe pattern demodulation. *Opt Laser Technol*
894 2011;43:72–81. doi:10.1016/j.optlastec.2010.05.007.
- 895 [43] Gdeisat MA, Abid A, Burton DR, Lalor MJ, Lilley F, Moore C, et al. Spatial and temporal
896 carrier fringe pattern demodulation using the one-dimensional continuous wavelet
897 transform: Recent progress, challenges, and suggested developments. *Opt Lasers Eng*
898 2009;47:1348–61. doi:10.1016/j.optlaseng.2009.07.009.
- 899 [44] Gdeisat MA, Burton DR, Lalor MJ. Spatial carrier fringe pattern demodulation by use of a
900 two-dimensional continuous wavelet transform. *Appl Opt* 2006;45:8722–32.
901 doi:10.1364/AO.45.008722.
- 902 [45] Li S, Su X, Chen W. Spatial carrier fringe pattern phase demodulation by use of a two-
903 dimensional real wavelet. *Appl Opt* 2009;48:6893–906. doi:10.1364/AO.48.006893.
- 904 [46] Li B, Tang C, Zhu X, Su Y, Xu W. Shearlet transform for phase extraction in fringe
905 projection profilometry with edges discontinuity. *Opt Lasers Eng* 2016;78:91–8.
906 doi:10.1016/j.optlaseng.2015.10.007.
- 907 [47] Lim WQ. The discrete shearlet transform: A new directional transform and compactly
908 supported shearlet frames. *IEEE Trans Image Process* 2010;19:1166–80.
909 doi:10.1109/TIP.2010.2041410.
- 910 [48] Huang NE, Shen Z, Long SR, Wu MC, Shih HH, Zheng Q, et al. The empirical mode
911 decomposition and the Hilbert spectrum for nonlinear and non-stationary time series
912 analysis. *Proc R Soc A Math Phys Eng Sci* 1998;454:903–95.
913 doi:10.1098/rspa.1998.0193.
- 914 [49] Goncalves P, Rilling G, Flandrin P. On empirical mode decomposition and its algorithms.
915 *IEEE-EURASIP Work Nonlinear Signal Image Process* 2003;3:8–11.

- 916 doi:10.1109/ICASSP.2008.4518437.
- 917 [50] Feng S, Chen Q, Zuo C, Sun J, Tao T, Hu Y. A carrier removal technique for Fourier
918 transform profilometry based on principal component analysis. *Opt Lasers Eng*
919 2015;74:80–6. doi:10.1016/j.optlaseng.2015.05.009.
- 920 [51] Posdamer J., Altschuler M. Surface measurement by space-encoded projected beam
921 systems. *Comput Graph Image Process* 1982;18:1–17. doi:10.1016/0146-664X(82)90096-
922 X.
- 923 [52] Sato K, Seiji I. Three-dimensional surface measurement by space encoding range imaging.
924 *J Robot Syst 2* 1985;2:27–39.
- 925 [53] Hall-Holt O, Rusinkiewicz S. Stripe boundary codes for real-time structured-light range
926 scanning of moving objects. *Proc Eighth IEEE Int Conf Comput Vision ICCV 2001*
927 2001;2. doi:10.1109/ICCV.2001.937648.
- 928 [54] Rusinkiewicz S, Hall-Holt O, Levoy M. Real-time 3D model acquisition. *ACM Trans*
929 *Graph* 2002;21. doi:10.1145/566654.566600.
- 930 [55] Quan C, He XY, Wang C, Tay CJ, Shang HM. Shape measurement of small objects using
931 LCD fringe projection with phase shifting. *Opt Commun* 2001;189:21–9.
- 932 [56] Huang PS, Zhang S. Fast three-step phase-shifting algorithm. *Appl Opt* 2006;45:5086–91.
933 doi:10.1364/AO.45.005086.
- 934 [57] Hu Y, Xi J, Chicharo J, Yang Z. Improved three-step phase shifting profilometry using
935 digital fringe pattern projection. *Proc. - Comput. Graph. Imaging Vis. Tech. Appl.*
936 *CGIV'06*, vol. 2006, 2006, p. 161–6. doi:10.1109/CGIV.2006.58.
- 937 [58] Takasaki H. Moiré topography. *Appl Opt* 1970;9:1467–72.
- 938 [59] Benoit P, Mathieu E, Hormière J, Thomas A. Characterization and control of
939 threedimensional objects using fringe projection techniques. *Nouv Rev d'Optique*
940 1975;6:67–86. doi:10.1088/0335-7368/6/2/301.
- 941 [60] Pirodda L. Shadow and Projection Moire Techniques for Absolute or Relative Mapping of
942 Surface Shapes. *Opt Eng* 1982;21 :640–9. doi:10.1117/12.7972959.
- 943 [61] Ryu W-J, Kang Y-J, Baik S-H, Kang S-J. A study on the 3-D measurement by using
944 digital projection moiré method. *Opt - Int J Light Electron Opt* 2008;119:453–8.
945 doi:10.1016/j.ijleo.2006.12.016.
- 946 [62] Buytaert JAN, Dirckx JJJ. Moiré profilometry using liquid crystals for projection and
947 demodulation. *Opt Express* 2008;16:179–93. doi:10.1364/OE.16.000179.
- 948 [63] Dirckx JJJ, Buytaert JAN, Van der Jeught S. Implementation of phase-shifting moiré
949 profilometry on a low-cost commercial data projector. *Opt Lasers Eng* 2010;48:244–50.
950 doi:10.1016/j.optlaseng.2009.03.013.
- 951 [64] Buytaert JAN, Dirckx JJJ. Phase-shifting Moiré topography using optical demodulation on
952 liquid crystal matrices. *Opt Lasers Eng* 2010;48:172–81.
953 doi:10.1016/j.optlaseng.2009.03.018.
- 954 [65] Engelhardt K. Acquisition of 3-D data by focus sensing utilizing the moire effect of CCD
955 cameras. *Appl Opt* 1991;30:1401–7. doi:10.1364/AO.30.001401.

- 956 [66] Zhang S, Huang P. High-Resolution, Real-time 3D Shape Acquisition. 2004 Conf Comput
957 Vis Pattern Recognit Work 2004. doi:10.1109/CVPR.2004.86.
- 958 [67] Jia P, Kofman J, English C. Multiple-step triangular-pattern phase shifting and the
959 influence of number of steps and pitch on measurement accuracy. *Appl Opt*
960 2007;46:3253–62. doi:10.1364/AO.46.003253.
- 961 [68] Jia P, Kofman J, English C. Error compensation in two-step triangular-pattern phase-
962 shifting profilometry. *Opt Lasers Eng* 2008;46:311–20.
963 doi:10.1016/j.optlaseng.2007.11.004.
- 964 [69] Zhang S, Yau S-T. High-speed three-dimensional shape measurement system using a
965 modified two-plus-one phase-shifting algorithm. *Opt Eng* 2007;46:113603.
966 doi:10.1117/1.2802546.
- 967 [70] Wizinowich PL. Phase shifting interferometry in the presence of vibration: a new
968 algorithm and system. *Appl Opt* 1990;29:3271–9. doi:10.1364/AO.29.003271.
- 969 [71] Zuo C, Chen Q, Gu G, Feng S, Feng F. High-speed three-dimensional profilometry for
970 multiply objects with complex shapes. *Opt Express* 2012;20:19493.
971 doi:10.1364/OE.20.019493.
- 972 [72] Ding Y, Xi J, Yu Y, Deng F. Absolute phase recovery of three fringe patterns with
973 selected spatial frequencies. *Opt Lasers Eng* 2015;70:18–25.
974 doi:10.1016/j.optlaseng.2014.12.024.
- 975 [73] Zhang S. Recent progresses on real-time 3D shape measurement using digital fringe
976 projection techniques. *Opt Lasers Eng* 2010;48:149–58.
977 doi:10.1016/j.optlaseng.2009.03.008.
- 978 [74] Wang Y, Zhang S, Oliver JH. 3D shape measurement technique for multiple rapidly
979 moving objects. *Opt Express* 2011;19:8539–45. doi:10.1364/OE.19.008539.
- 980 [75] Zhang S. Flexible 3D shape measurement using projector defocusing: extended
981 measurement range. *Opt Lett* 2010;35:934–6. doi:10.1364/OL.35.000934.
- 982 [76] Kim E-H, Hahn J, Kim H, Lee B. Profilometry without phase unwrapping using multi-
983 frequency and four-step phase-shift sinusoidal fringe projection. *Opt Express*
984 2009;17:7818–30. doi:10.1364/OE.17.007818.
- 985 [77] Wang Y, Zhang S. Superfast multifrequency phase-shifting technique with optimal pulse
986 width modulation. *Opt Express* 2011;19:5149–55. doi:10.1364/OE.19.005149.
- 987 [78] Karpinsky N, Hoke M, Chen V, Zhang S. High-resolution, real-time three-dimensional
988 shape measurement on graphics processing unit. *Opt Eng* 2014;53:024105.
- 989 [79] Lei Z, Wang C, Zhou C. Multi-frequency inverse-phase fringe projection profilometry for
990 nonlinear phase error compensation. *Opt Lasers Eng* 2015;66:249–57.
991 doi:10.1016/j.optlaseng.2014.09.018.
- 992 [80] García-Isáis C a., Alcalá Ochoa N. One shot profilometry using a composite fringe
993 pattern. *Opt Lasers Eng* 2014;53:25–30. doi:10.1016/j.optlaseng.2013.08.006.
- 994 [81] García-Isáis CA, Alcalá Ochoa N. One shot profilometry using phase partitions. *Opt*
995 *Lasers Eng* 2015;68:111–20. doi:10.1016/j.optlaseng.2014.12.016.
- 996 [82] Guan C, Hassebrook L, Lau D. Composite structured light pattern for three-dimensional

- 997 video. *Opt Express* 2003;11:406–17. doi:10.1364/OE.11.000406.
- 998 [83] Koninckx TP, Geys I, Jaeggli T, Van Gool L. A graph cut based adaptive structured light
999 approach for real-time range acquisition. *Proc. - 2nd Int. Symp. 3D Data Process. Vis.*
1000 *Transm. 3DPVT* 2004, 2004, p. 413–21. doi:10.1109/TDPVT.2004.1335268.
- 1001 [84] Koninckx TP, Van Gool L. Real-time range acquisition by adaptive structured light. *IEEE*
1002 *Trans Pattern Anal Mach Intell* 2006;28:432–45. doi:10.1109/TPAMI.2006.62.
- 1003 [85] Koninckx TP, Griesser A, Van Gool L. Real-time range scanning of deformable surfaces
1004 by adaptively coded structured light. *Fourth Int Conf 3-D Digit Imaging Model 2003*
1005 *3DIM 2003 Proceedings* 2003. doi:10.1109/IM.2003.1240262.
- 1006 [86] Griesser A, Koninckx TP, Van Gool L. Adaptive real-time 3D acquisition and contour
1007 tracking within a multiple structured light system. *12th Pacific Conf Comput Graph Appl*
1008 *2004 PG 2004 Proceedings* 2004:361–70. doi:10.1109/PCCGA.2004.1348367.
- 1009 [87] Zhao M, Huang L, Zhang Q, Su X, Asundi A, Kemao Q. Quality-guided phase
1010 unwrapping technique: comparison of quality maps and guiding strategies. *Appl Opt*
1011 2011;50:6214–24.
- 1012 [88] Lu Y, Wang X, Zhong X, He G, Liu Y, Zheng D. A new quality map for quality-guided
1013 phase unwrapping. *Chinese Opt Lett* 2004;2:698–700.
- 1014 [89] Su X. Reliability-guided phase unwrapping algorithm: a review. *Opt Lasers Eng*
1015 2004;42:245–61. doi:10.1016/j.optlaseng.2003.11.002.
- 1016 [90] Herráez MA, Burton DR, Lalor MJ, Gdeisat MA. Fast two-dimensional phase-unwrapping
1017 algorithm based on sorting by reliability following a noncontinuous path. *Appl Opt*
1018 2002;41:7437–44.
- 1019 [91] Zhang S, Li X, Yau S. Multilevel quality-guided phase unwrapping algorithm for real-
1020 time three-dimensional shape reconstruction. *Appl Opt* 2007;46:50–7.
- 1021 [92] Nico G, Palubinskas G, Datcu M. Bayesian approaches to phase unwrapping: theoretical
1022 study. *IEEE Trans Signal Process* 2000;48. doi:10.1109/78.863057.
- 1023 [93] Marroquin JL, Tapia M, Rodriguez-Vera R, Servin M. Parallel algorithms for phase
1024 unwrapping based on Markov random field models. *J Opt Soc Am A Opt Image Sci Vis*
1025 1995;12:2578–85.
- 1026 [94] Xu W, Gumming L. A region-growing algorithm for InSAR phase unwrapping. *IEEE*
1027 *Trans Geosci Remote Sens* 1999;37:124–34. doi:10.1109/36.739143.
- 1028 [95] Schwartzkopf W, Milner TE, Ghosh J, Evans BL, Bovik a. C. Two-dimensional phase
1029 unwrapping using neural networks. *Image Anal Interpret 2000 Proceedings 4th IEEE*
1030 *Southwest Symp* 2000:274–7.
- 1031 [96] Karout SA, Gdeisat MA, Burton DR, Lalor MJ. Two-dimensional phase unwrapping
1032 using a hybrid genetic algorithm. *Appl Opt* 2007;46:730–43. doi:10.1364/AO.46.000730.
- 1033 [97] Fornaro G, Franceschetti G, Lanari R. Interferometric SAR phase unwrapping using
1034 Green's formulation. *IEEE Trans Geosci Remote Sens* 1996;34:720–7.
1035 doi:10.1109/36.499751.
- 1036 [98] Suksmono AB, Hirose A. Improving phase-unwrapping result of InSAR images by
1037 incorporating the fractal model. *Proc 2003 Int Conf Image Process (Cat No03CH37429)*

- 1038 2003;2. doi:10.1109/ICIP.2003.1246809.
- 1039 [99] Carballo GF, Fieguth PW. Probabilistic cost functions for network flow phase
1040 unwrapping. *IEEE Trans Geosci Remote Sens* 2000;38:2192–201.
1041 doi:10.1109/36.868877.
- 1042 [100] Ghiglia DC, Mastin GA, Romero LA. Cellular-automata method for phase unwrapping. *J*
1043 *Opt Soc Am A* 1987;4:267–80.
- 1044 [101] Ghiglia DC, Romero LA. Minimum L-p-norm two-dimensional phase unwrapping. *J Opt*
1045 *Soc Am A* 1996;13:1999. doi:10.1364/JOSAA.13.001999.
- 1046 [102] Chen CW, Zebker HA. Two-dimensional phase unwrapping with use of statistical models
1047 for cost functions in nonlinear optimization. *J Opt Soc Am A* 2001;18:338.
1048 doi:10.1364/JOSAA.18.000338.
- 1049 [103] Cusack R, Papadakis N. New robust 3-D phase unwrapping algorithms: application to
1050 magnetic field mapping and undistorting echoplanar images. *Neuroimage* 2002;16:754–
1051 64. doi:10.1006/nimg.2002.1092.
- 1052 [104] Jenkinson M. Fast, automated, N-dimensional phase-unwrapping algorithm. *Magn Reson*
1053 *Med* 2003;49:193–7. doi:10.1002/mrm.10354.
- 1054 [105] Van der Jeught S, Sijbers J, Dirckx J. Fast Fourier-Based Phase Unwrapping on the
1055 Graphics Processing Unit in Real-Time Imaging Applications. *J Imaging* 2015;1:31–44.
1056 doi:10.3390/jimaging1010031.
- 1057 [106] Read P, Meyer M-P. Restoration of motion picture film. Butterworth-Heinemann; 2000.
- 1058 [107] Huang PS, Zhang C, Chiang F-P. High-speed 3-D shape measurement based on digital
1059 fringe projection. *Opt Eng* 2003;42:163. doi:10.1117/1.1525272.
- 1060 [108] Zhang S, Huang P. High-resolution, real-time three-dimensional shape measurement. *Opt*
1061 *Eng* 2006;45:123601–8.
- 1062 [109] Pan J, Huang PS, Zhang S, Chiang F-P. Color N-Ary Gray Code for 3-D Shape
1063 Measurement. *ICEM12- 12th Int Conf Exp Mech* 2004.
- 1064 [110] Zhang S, Royer D, Yau S-T. GPU-assisted high-resolution, real-time 3-D shape
1065 measurement. *Opt Express* 2006;14:9120–9. doi:10.1364/OE.14.009120.
- 1066 [111] Liu K, Wang Y, Lau DL, Hao Q, Hassebrook LG. Dual-frequency pattern scheme for
1067 high-speed 3-D shape measurement. *Opt Express* 2010;18:5229–44.
1068 doi:10.1364/OE.18.005229.
- 1069 [112] Van der Jeught S, Soons J, Dirckx JJJ. Real-time microscopic phase-shifting profilometry.
1070 *Appl Opt* 2015;54:4953–9.
- 1071 [113] Nguyen H, Nguyen D, Wang Z, Kieu H, Le M. Real-time, high-accuracy 3D imaging and
1072 shape measurement. *Appl Opt* 2015. doi:10.1364/ao.54.0000a9.
- 1073 [114] Turk G, Levoy M. Zippered polygon meshes from range images. *Proc 21st Annu Conf ...*
1074 1994;94pp:311–8. doi:10.1145/192161.192241.
- 1075 [115] Soucy M, Laurendeau D. Multi-resolution surface modeling from multiple range views.
1076 *Proc 1992 IEEE Comput Soc Conf Comput Vis Pattern Recognit* 1992.
1077 doi:10.1109/CVPR.1992.223166.

- 1078 [116] Han TD, Abdelrahman TS. HiCUDA: High-level GPGPU programming. IEEE Trans
1079 Parallel Distrib Syst 2011;23:78–90. doi:10.1109/TPDS.2010.62.
- 1080 [117] Gong Y, Zhang S. Ultrafast 3-D shape measurement with an off-the-shelf DLP projector.
1081 Opt Express 2010;18:19743–54.
- 1082 [118] Su X-Y, Zhou W-S, von Bally G, Vukicevic D. Automated phase-measuring profilometry
1083 using defocused projection of a Ronchi grating. Opt Commun 1992;94:561–73.
1084 doi:10.1016/0030-4018(92)90606-R.
- 1085 [119] Lei S, Zhang S. Flexible 3-D shape measurement using projector defocusing. Opt Lett
1086 2009;34:3080–2. doi:10.1364/OL.34.003080.
- 1087 [120] Takei J, Kagami S, Hashimoto K. 3,000-fps 3-D Shape Measurement Using a High-Speed
1088 Camera-Projector System. Discovery 2007:3211–6.
- 1089 [121] Zhang S, Van Der Weide D, Oliver J. Superfast phase-shifting method for 3-D shape
1090 measurement. Opt Express 2010;18:9684–9. doi:10.1364/OE.18.009684.
- 1091 [122] Zuo C, Chen Q, Gu G, Feng S, Feng F, Li R, et al. High-speed three-dimensional shape
1092 measurement for dynamic scenes using bi-frequency tripolar pulse-width-modulation
1093 fringe projection. Opt Lasers Eng 2013;51:953–60. doi:10.1016/j.optlaseng.2013.02.012.
- 1094 [123] Gao W, Huyen NTT, Loi HS, Kemao Q. Real-time 2D parallel windowed Fourier
1095 transform for fringe pattern analysis using Graphics Processing Unit. Opt Express
1096 2009;17:23147–52. doi:10.1364/OE.17.023147.
- 1097 [124] Chen L-C, Nguyen XL, Zhang F-H, Lin T-Y. High-speed Fourier transform profilometry
1098 for reconstructing objects having arbitrary surface colours. J Opt 2010;12:095502.
1099 doi:10.1088/2040-8978/12/9/095502.
- 1100 [125] Hu Y, Xi J, Li E, Chicharo J, Yang Z, Yu Y. A calibration approach for decoupling colour
1101 cross-talk using nonlinear blind signal separation network. Conf. Optoelectron.
1102 Microelectron. Mater. Devices, Proceedings, COMMAD, 2005, p. 265–8.
1103 doi:10.1109/COMMAD.2004.1577541.
- 1104 [126] Hu Y, Xi J, Chicharo J, Yang Z. Blind color isolation for color-channel-based fringe
1105 pattern profilometry using digital projection. J Opt Soc Am A Opt Image Sci Vis
1106 2007;24:2372–82. doi:10.1364/JOSAA.24.002372.

1107

1108

1109 Sam Van der Jeught was born in Antwerp, Belgium, in 1987. He graduated as master in Physics
1110 in 2010 from the University of Antwerp, where he researched new ways of accelerating the
1111 digital signal processing algorithms involved in optical coherence tomography in a joint
1112 collaboration between the Laboratory of Biomedical Physics (BIMEF) and the University of
1113 Kent, UK. As a Marie Curie fellow, he was able to work at the Applied Optics Group (AOG) at
1114 the University of Kent for a period of ten months. He received his degree of PhD in Science:
1115 Physics in 2015 at the University of Antwerp for the dissertation entitled “Optical techniques for
1116 real-time morphology measurement of the tympanic membrane”. He is currently researching new
1117 optical methods for measuring human eardrum shape in real-time and in-vivo as a post-doctoral
1118 fellow with funding from the Research Foundation - Flanders (FWO).



1119

1120

1121 Joris J.J. Dirckx was born in Antwerp , Belgium , in 1960. He graduated in Physics and in
1122 Didactics at the University of Antwerp , taught physics and mathematics in high school, and then
1123 became assistant at the University of Antwerp . In 1991 he obtained the PhD in Physics, with the
1124 dissertation “Automated moiré topography and its use for shape and deformation measurements
1125 of the eardrum”. From 1992 to 1993 he worked as scientific advisor for the government (IWT),
1126 where he assessed and audited major industrial research projects, with a total project portfolio of
1127 over 10 million Euros. In 1994 he returned to research and worked at the ENT department of St.
1128 Augustinus hospital as clinical audiologist, and performed research on oto-acoustic emissions
1129 and cochlear implants. In 1996 he joined the University of Antwerp as post-doc researcher, and
1130 was appointed lecturer in physics in 2000. He became professor in 2003, and is now director of
1131 the laboratory of Biomedical Physics and full professor in the Department of Physics. He teaches
1132 courses in general physics for pharmacy, biology and biochemistry students, physics of optical
1133 microscopy, and courses in practical holography and biomedical imaging for physics students.



1134

1135

1136